Electrochimica Acta 56 (2011) 6722–6731

Contents lists available at ScienceDirect

Electrochimica Acta

journal homepage: www.elsevier.com/locate/electacta

Electrochemical properties of electrospun Cu_xO ($x = 1, 2$)-embedded carbon nanofiber with EXAFS analysis

Hong-Ryun Jung[a], Sung June Cho[a,b], Kyung Nam Kim[c], Wan-Jin Lee[a,b,*]

[a] School of Applied Chemical Engineering, Chonnam National University, Gwangju 500-757, Republic of Korea
[b] Center for Functional Nano Fine Chemicals, Chonnam National University, Gwangju 500-757, Republic of Korea
[c] Department of Chemical and Environmental Engineering, Daebul University, Jeonnam 530-702, Republic of Korea

ARTICLE INFO

Article history:
Received 9 March 2011
Received in revised form 24 April 2011
Accepted 6 May 2011
Available online 27 May 2011

Keywords:
Copper oxide
Carbon nanofibers
Electrospinning
Lithium ion battery
Extended X-ray absorption fine structure

ABSTRACT

The Cu_xO ($x = 1, 2$)-embedded carbon nanofibers (Cu_xO/CNF) were prepared by electrospinning of the composite solutions of Cu(II) acetate, PAN (polyacrylonitrile) and PVP (polyvinylpyrrolidone), and subsequent stabilization and carbonization. The structure of Cu_2O/CNF is largely dependent on the carbonization temperature. The Cu_xO/CNF-700 has the disordered CuO structure, while the Cu_xO/CNF-800 has the intermediate structure between the disordered CuO and Cu_2O. The structural change in the CNF prepared by electrospinning and optimum thermal treatment leads to excellent electrochemical properties. The CNF plays an important role as buffering agent to prevent Cu_xO particles from agglomerating. Besides, the aligned CNF with high electrical conductivity leads to the occurrence of Cu nano-particles in the discharging process, and it serves to convert Li_2O into Li in the charging process. Both Cu_xO/CNF-700 and Cu_xO/CNF-800 exhibit high specific discharge capacity, exceptional cycle retention, and excellent reversible capacity even in initial cycle, while Cu_xO/CNF-900 shows bad electrochemical performance.

1. Introduction

The search for alternative anodic materials to replace graphite (372 mAh g^{-1}) in lithium ion batteries is being attracted as a topic of substantial issue because of the importance of hybrid cars. The 3*d* transition metal oxides (M_xO_y, M = Co, Cu, Fe, Mn) [1–4] are promising anode materials due to their high specific capacity and safe operation. Among them, Cu_xO has advantages of high theoretical capacity (CuO: 670 mAh g^{-1}, Cu_2O: 380 mAh g^{-1}), inexpensive production, and non-toxicity [5–7]. However, these materials have a critical problem in commercializing as alternative anodic materials because of large irreversible capacity at initial cycle originated from the incomplete decomposition of Li_2O, incurring the reduced electric conductivity during Li ion insertion and extraction. In the past decade, many researches regarding Cu_xO have been diversely conducted to increase the specific capacity, long-term cyclic performance, and reversible capacity by preparing the diverse structure such as hollow type [8,9], nano-film [10,5], nano-flower [11], nano-tube [6], and nano-ribbons [12], and by synthesizing nanocomposites such as graphene–Cu_xO [13] and Cu_xO/CNT [14,15]. In spite of such efforts, the Cu_xO fabricated by diverse methods is still restricted due to low specific capacity and bad cycle retention. For instance, the specific capacity of these materials easily decreases to below 400 mAh g^{-1} within 50 cycles with the increase of cycle [16,17]. Accordingly, the new method is urgently demanded in order to improve electrochemical performance by preparing well-dispersed and size-constrained Cu_xO as the alternative carbonaceous anode materials.

Electrospinning is a unique method to make metal oxide well-dispersed within non-woven composite nanofibers, resulting in metal oxide-embedded carbon nanofibers through the process of thermal treatment. These nanofiber composites possess high surface area, highly porous structures, and easy electron pathways because of the interconnected morphology of the metal oxide-embedded carbon nanofibers [18,19]. Little attention has been focused on the methods of enhancing the electrochemical performance by preparing electrospun nano-metal oxide-embedded carbon nanofibers composites. Moreover, the relationship between electrochemical performance and the fine structure of electrospun Cu_xO-embedded CNF has not been reported. The extended X-ray absorption fine structure (EXAFS) analysis is a useful technique to analyze fine structure, including bonding length, coordination number, disorder and atomic species around X-ray absorbing atom of the nano-size materials [20,21]. As for metal oxide-embedded carbon nanofiber, the EXAFS study plays an important role to verify the state of metal oxide with carbonizing temperature and the relationship between fine structure and electrochemical property.

* Corresponding author: School of Applied Chemical Engineering, Chonnam National University, Gwangju 500-757, Republic of Korea. Tel.: +82 62 530 1895; fax: +82 62 530 1889.
E-mail address: wjlee@jnu.ac.kr (W.-J. Lee).

0013-4686/$ – see front matter © 2011 Elsevier Ltd. All rights reserved.
doi:10.1016/j.electacta.2011.05.068

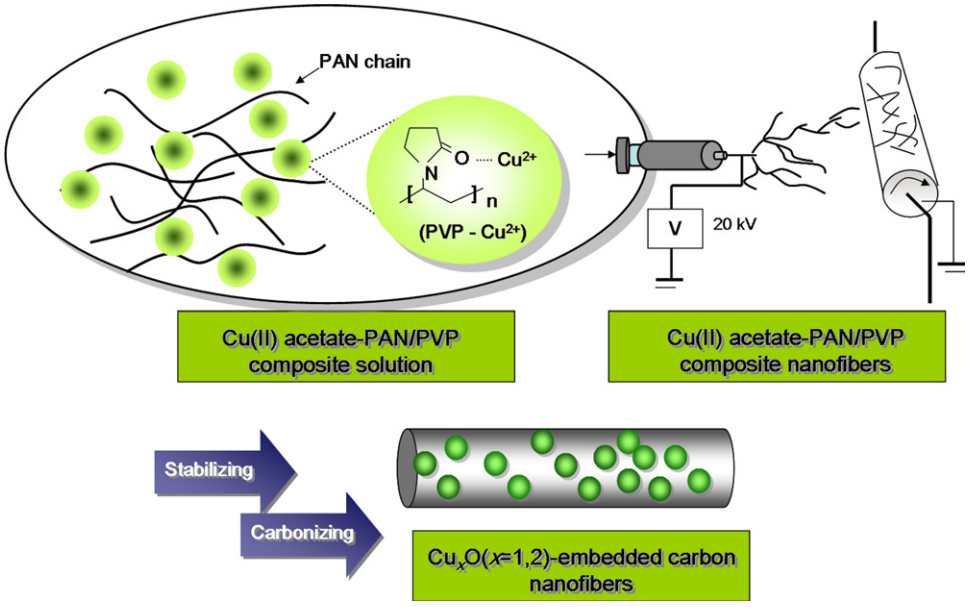

Scheme 1. Illustration for the preparation of Cu_xO-embedded carbon nanofiber (Cu_xO/CNF).

An objective of this study is to develop noble Cu_xO-embedded carbon nanofibers composite as alternative anodic materials with higher reversible capacities and excellent cyclic performance. The Cu_xO-embedded carbon nanofibers composites are prepared by electrospinning and thermal treatment. The synergistic effect by combination of electrospinning and optimum thermal treatment is the key of preparing carbon nanofiber composites dispersed with Cu_xO as nanoparticles. The fine structure of Cu_xO-embedded within carbon nanofibers were scrutinized by extended X-ray absorption fine structure (EXAFS).

2. Experimental

2.1. Materials

Pure Cu_2O powder (particle size *ca.* 5 μm) and polyacrylonitrile (PAN, M_w = 150,000) as a carbon precursor were purchased from Aldrich Chemical Co. The Cu(II) acetate (M_w = 181.63, 99.999%; Aldrich Chemical Co.) was used as the precursor for Cu_2O and CuO. N,N-dimethylformamide (DMF, Aldrich Chemical Co.) and polyvinylpyrrolidone (PVP, M_w = 1,300,000; Alfa Aesar Co.) were used as main solvent and a stabilizer, respectively. PVP plays important roles in distributing the Cu(II) acetate as it acts as a stabilizer. It promotes the formation of Cu_2O and CuO and excludes the formation of Cu metal by providing an oxygen-rich environment in the carbon nanofibers.

2.2. Preparation of Cu_xO-embedded carbon nanofibers electrode

The non-woven nanofiber webs were prepared by electrospinning an 8 wt% PAN/PVP blend solution of 4 wt% PAN and 4 wt% PVP in N,N-dimethylformamide. The carbon nanofibers (CNF) were prepared through the process of stabilization and carbonization. In detail, the stabilization was carried out by holding it for 5 h after elevating temperature to 230 °C at the rate of 1 °C min^{-1} in atmosphere, and the carbonization was executed by holding it for 1 h after heating to 800 °C at the rate of 5 °C min^{-1} in nitrogen. The Cu(II) acetate embedded non-woven composite nanofibers web were prepared by electrospinning of the composite solution, composed of 0.103 g Cu(II) acetate and the above PAN/PVP blend solution. The Cu_xO-embedded carbon nanofibers (Cu_xO/CNF) were then synthesized during the stabilization and subsequent carbonization at 700, 800, and 900 °C, respectively. The ratio of Cu_xO to CNF was fixed at 3:7 after burning off the non-woven composite nanofibers. The as-received Cu_2O powder was labeled as pure Cu_2O, the electrospun carbon nanofibers prepared at 800 °C were labeled as pure CNF, and the electrospun Cu_xO/CNF composites were labeled with their carbonization temperature (°C) appended: e.g. Cu_xO/CNF-700.

The electrochemical properties were evaluated by galvanostatic discharge/charge test to use the 2032 coin cell (Hohsen Corp.). The coin cell was composed of two electrodes of working electrode and counter electrode. The Cu_xO/CNF as a working electrode was used by drying for 12 h at 120 °C in a vacuum oven to completely remove the water. Lithium foil was used as a counter electrode. Polypropylene film (Celgard 2400) and 1 M $LiPF_6$ + EC/DMC (1:1, v/v) (Techno Semichem Co.) were used as a separator and an electrolyte, respectively. The coin cell was assembled in Ar-filled grove box. The discharge-charge properties of the samples were measured at a current density of 0.5 mA/cm^2 over the voltage range of 0.02–2.8 V.

2.3. Characterization

The morphologies of pure Cu_2O and the Cu_xO/CNFs were observed by field emission scanning electron microscopy (FE-SEM, S-4700, Hitachi, Japan). The size and degree of dispersion of the Cu_xO nanoparticles in each carbon nanofiber matrix were measured by high resolution transmission electron microscopy (HR-TEM, JEM-2200FS, JEOL, USA). The crystallization results for pure Cu_2O and Cu_xO-embedded CNFs were analyzed by the X-ray diffraction (XRD, D/MAX Uitima III, Rigaku, Japan). The extended X-ray absorption fine structure (EXAFS) measurements were carried out using an XAFS Beamline with a Si(1 1 1) double crystal monochrometer at the Pohang Accelerator Laboratory (PAL; 2.5 GeV with the stored currents 130–200 mA). The Cu–K edge spectra were recorded in transmittance mode at room temperature. The EXAFS data were analyzed to fit the experimental EXAFS spectra to theoretical values obtained by an IFEFFIT program based on FEFF8. The electrical conductivities of samples were measured by a four-probe method. The charge–discharge tests were conducted using a battery cycler system (WBCS 3000, Won-A Tech. Co., Korea).

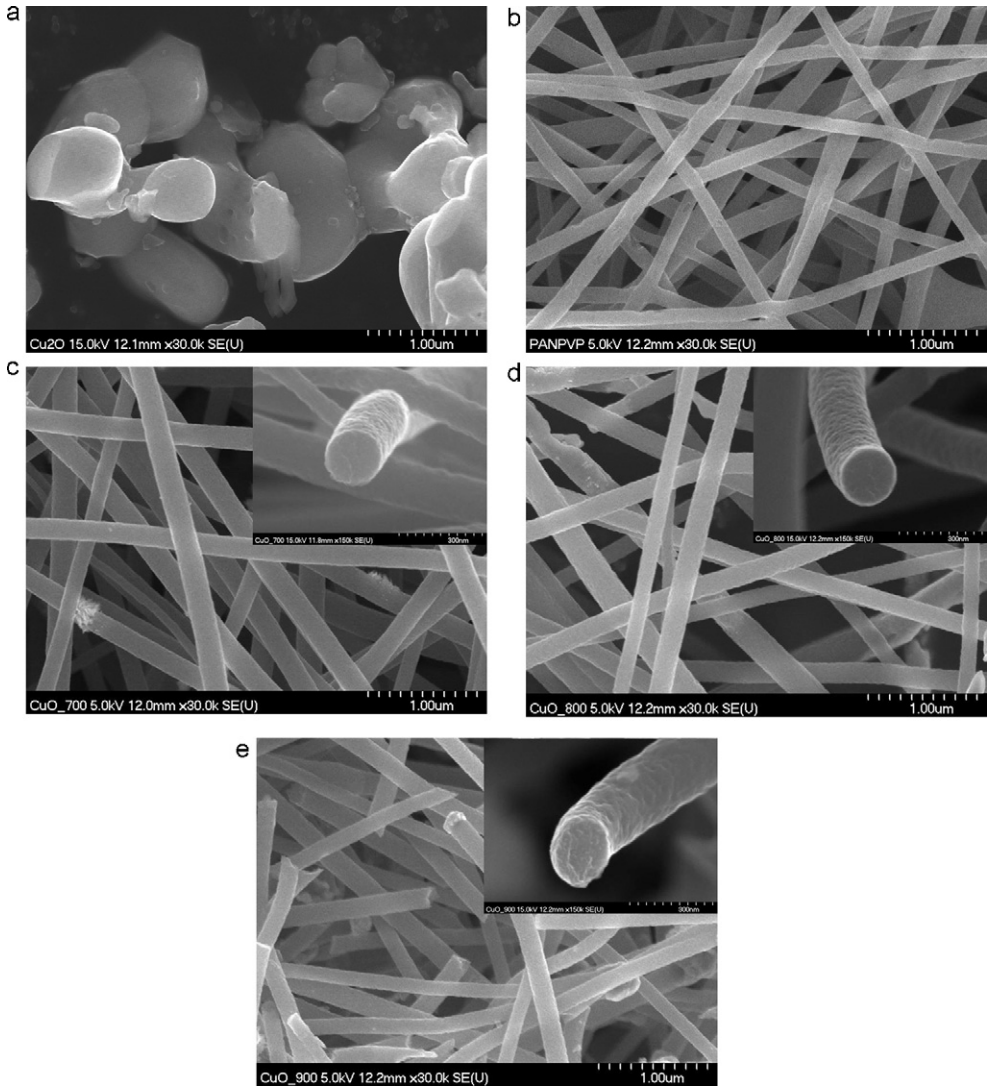

Fig. 1. SEM images of pure Cu_2O, pure CNF, Cu_xO/CNFs with various temperatures: (a) pure Cu_2O, (b) pure CNFs, (c) Cu_xO/CNF-700, (d) Cu_xO/CNF-800, and (e) Cu_xO/CNF-900.

3. Results and discussion

Scheme 1 represents the preparation of the Cu_xO-embedded carbon nanofibers. First, the electrospun non-woven Cu(II) acetate-PAN/PVP composite nanofibers are formed as the type of PVP-Cu^{2+} caused by the interaction between the carbonyl oxygen of PVP and the Cu^{2+} of Cu(II) acetate. The carbon nanofibers with well-distributed Cu_xO are then formed by optimum thermal process.

Fig. 1 shows the SEM images of the surfaces of pure Cu_2O and pure CNF carbonized at 800 °C, and the various Cu_xO/CNFs carbonized at 700, 800, and 900 °C. The undefined x in Cu_xO represents the transformations between CuO and Cu_2O with the change of temperature, as mentioned in the analysis of XRD and EXAFS later on. As shown in Fig. 1(a), pure Cu_2O powder forms the spherical-like shape to be agglomerated, showing random particle distribution in the range of 500 nm to 3 μm in diameter. On the other hand, pure CNF and Cu_xO/CNFs are partially aligned along the winding direction of the drum winder, representing a porous, fully interconnected structure between fibers. As for Fig. 1(b), the fiber diameter of pure CNF (800 °C) is about 140 nm in average diameter, while that of Cu_xO/CNF-800 is slightly thicker than pure CNF as about 170 nm. In Cu_xO/CNF, with the increase of temperature from 700 to 900 °C, the average diameter of fiber for Cu_xO/CNF is gradually decreased from 200 nm to 150 nm. The Cu_xO/CNF-900 is partially broken because the Cu_xO particles in the CNF became agglomerated at the high temperature. The fiber diameter of Cu_xO/CNF is involved in degree of distribution for Cu_xO in CNF. With the increase of temperature from 700 to 800 °C, the fiber diameter of Cu_xO/CNFs is reduced from 200 to 170 nm. The decrease of fiber diameter in Cu_xO/CNFs is due to removal of non-carbon elements with increasing carbonizing temperature. The fiber diameter of Cu_xO/CNF-700 and Cu_xO/CNF-800 is only slightly increased compared to pure CNF (140 nm) prepared at 800 °C, because the Cu_xO is well distributed as a few nanosize in CNF. On the other hand, the fiber diameter for Cu_xO/CNF-900 is decreased as 150 nm due to more burn-off of CNF, but high carbonation temperature brings about the agglomeration of Cu_xO, leading to the deterioration of electrochemical performance. The degree of distribution for Cu_xO in CNF with temperatures is confirmed by HR-TEM later on.

Fig. 2 shows the XRD patterns of pure Cu_2O, pure CNF and the Cu_xO/CNFs. The crystallization peaks of pure Cu_2O are observed at $2\theta = 29°$, 36°, 42°, 61° and 73°, corresponding to the (1 1 0), (1 1 1), (2 0 0), (2 2 0), and (3 1 1) plane, respectively, indicating a *Pn*3*m* space group (JCPDS 05-0667) with high intensity. The pure CNF shows the typical amorphous structure. The structure of Cu_xO/CNF shows diverse structures with increasing temperature. The Cu_xO/CNF-700 exhibits two crystal structures: CuO (JCPDS 48-1548), with peaks at $2\theta = 35.4°$ and 38.5°, and a very weak Cu_2O

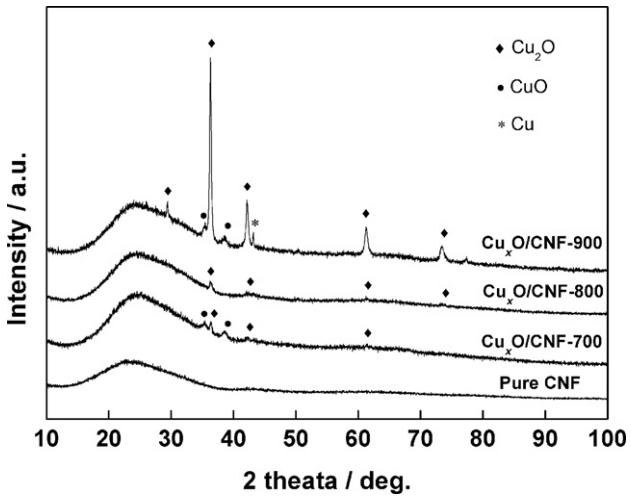

Fig. 2. XRD patterns Cu_xO/CNFs with various temperatures.

(JCPDS 05-0667) structure, with peaks at $2\theta = 36.3^\circ$ and 42.16°. The Cu_xO/CNF-800 shows small peaks relating to Cu_2O (JCPDS 05-0667) at $2\theta = 36.2^\circ$ and 42.16°. The Cu_xO/CNF-900 exhibits three structures: Cu_2O (JCPDS 05-0667), CuO (JCPDS 48-1548), and Cu (JCPDS 04-0836). The Cu_2O is strong peaks at 29.36°, 36.3°, 42.16°, 61.3°, and 73.4°, the CuO shows two weak peaks at $2\theta = 35.4^\circ$ and 38.6° and pure Cu displays a small peak at $2\theta = 43.1^\circ$. At carbonization temperatures of 700 and 800 °C, the crystal structures shows very weak peaks, suggesting that Cu_xO is well distributed as nanoparticles within the carbon fibers. However, the crystal structure of Cu_2O in Cu_xO/CNF-900 is well developed and exhibits a very strong peak. The CuO and pure Cu of Cu_xO/CNF-900 are also formed through the decomposition of Cu_2O, although they display very weak peaks [22,23].

Fig. 3 shows the HR-TEM images of the various Cu_xO/CNFs carbonized at 700, 800, and 900 °C, respectively, representing the sizes and the distributions and lattice spacing of Cu_xO particles. The Cu_xO/CNF-700, (Fig. 3(a)) has small (<4 nm), well-distributed Cu_xO particles. The Cu_xO particles in Cu_xO/CNF-800 are slightly larger, ranging from 4 to 10 nm in size. On the other hand, the Cu_xO particles for Cu_xO/CNF-900 are agglomerated within carbon nanofibers as over 100 nm in size. The Cu_xO particles in the Cu_xO/CNFs are much smaller than those of pure Cu_2O, because the carbon nanofibers play an important role as a buffering agent that prevents Cu_xO particles from agglomerating. The agglomeration of the Cu_xO particles at increased carbonization temperature brings about the reduction of electrochemical performance by inducing the decrease of the electrochemical active sites.

The extended X-ray absorption fine structure (EXAFS) analysis can provide information of bonding lengths (R), coordination number (CN), disorder (Debye–Waller factor, σ^2) and atomic species around the X-ray absorbing atoms. The quantitative results of these obtained from curve fitting radial distribution functions are listed in Table 1. The electrospun non-woven Cu(II) acetate-based PAN/PVP composite nanofibers are formed as PVP-Cu^{2+}, that is, the interactions between the carbonyl oxygen of PVP and the Cu^{2+} of Cu(II) acetate because PVP is used as a stabilizer [24–26]. The EXAFS results confirm that the electrospun non-woven Cu(II) acetate-based PAN/PVP composite nanofibers is synthesized as the diverse shape of CuO/CNF, and Cu_2O/CNF composites with the increase of carbonizing temperature [27–29].

Fig. 4(a) shows the result of X-ray absorption near edge spectra (XANES), offering the information of chemical state. The XANES curves for Cu_xO/CNF-700 and Cu_xO/CNF-800 are similar without transition of 1s to 4p, while that of Cu_xO/CNF-900 distinctly shows such transitions [30–32]. Fig. 4(b) represents the plot of the $k^3\chi(k)$, the normalized absorption coefficient, with the wave vector (k^3-weighted EXAFS) in the k-space of 2–13 $Å^{-1}$. The Cu_xO/CNF composite nanofibers are compared with pure Cu_2O and pure CuO samples. The Cu_xO/CNF-700 shows similar absorptive behavior to pure CuO, while the Cu_xO/CNF-800 shows similar patterns to pure CuO and pure Cu_2O at 5 and 7.8 $Å^{-1}$. The Cu_xO/CNF-900 shows nearly analogous behavior to pure Cu_2O. This behavior provides important information that the CuO in carbon nanofiber is transformed into Cu_2O in carbon nanofiber with the increase of temperature [24,33]. The higher carbonization temperature helps to be favorable condition for Cu_2O formation because the oxygen in carbon nanofiber is continuously eliminated. Fig. 4(c) represents the magnitude of the Fourier transformation with the distance from absorbing atom for pure CuO, pure Cu_2O and Cu_xO/CNFs with temperatures. The information containing the parameter of fine structure such as the bond length (R) and coordination number (CN) for pure CuO and pure Cu_2O [34] is required to obtain the transformation of structure for all Cu_xO/CNFs. For pure CuO, the R and CN of the first shell of Cu–O are 1.86 Å and 2, and 1.96 Å and 2, respectively, those of the second shell of Cu–O are 2.77 Å and 2, and those of the third shell of Cu–Cu are 2.90 Å and 10. On the other hand, for pure Cu_2O, the R and CN of the first shell of Cu–O are 1.85 Å and 2, those of the second shell of Cu–Cu are 3.07 Å and 12, and those of the third shell of Cu–O are 3.59 Å and 6. For the Cu_xO/CNF-700, the R and CN of the first shell corresponding to Cu–O are 1.88 Å and 1.99 Å with CN of 2 and 1.8, those of the second equivalent to Cu–O are 2.78 Å and 0.8, and those of the third shell matching to Cu–Cu are 2.94 Å and 1.8, and 3.08 Å and 1.7. The Cu_xO/CNF-700 possesses a CuO disordered structure by the decrease of CN as the shell increases. Compared with the structure of pure CuO, the number of oxygen in first and second shell is less than 0.2 and 1.2, respectively, and the number of Cu in third shell is insufficient 5.8 as well. This transformation occurs because CNF hinders the formation of regular Cu_xO structures, implying the good distribution of free Cu atoms in the second and higher shells. In the view

Table 1
Structural parameters of various Cu_xO/CNFs obtained from the curve fitting of EXAFS spectra.

Sample	Atomic pair	CN	R (Å)	$\Delta\sigma^2$ (Å^2)	ΔE_0 (eV)
CuO-ref.	Cu–O	2.0	1.86	0.00413	3.64
	Cu–O	2.0	1.96	0.00075	3.92
	Cu–O	2.0	2.77	0.00695	11.41
	Cu–Cu	4.0	2.90	0.0075	10.08
	Cu–Cu	4.0	3.00	0.0061	−2.22
	Cu–Cu	2.0	3.17	0.0031	−0.67
Cu_xO/CNF-700	Cu–O	2.0	1.88	0.00072	6.58
	Cu–O	1.8	1.99	0.00068	6.30
	Cu–O	0.8	2.78	0.0079	11.83
	Cu–Cu	1.8	2.94	0.0080	9.36
	Cu–Cu	1.7	3.08	0.0067	−2.99
	Cu–Cu	0.7	3.19	0.0035	−26.47
Cu_xO/CNF-800	Cu–O	1.7	1.88	0.0008	5.12
	Cu–O	1.4	1.99	0.0061	−0.07
	Cu–O	0.6	2.81	0.0061	13.45
	Cu–Cu	2.6	2.94	0.0081	7.52
	Cu–Cu	2.7	3.08	0.0068	−4.61
	Cu–Cu	1.2	3.19	0.0036	−28.87
Cu_xO/CNF-900	Cu–O	2.4	1.86	0.0043	6.74
	Cu–Cu	12.0	3.07	0.0077	13.35
	Cu–O	4.8	3.59	0.0077	7.61
Cu_2O-ref.	Cu–O	2	1.85	0.0020	6.22
	Cu–Cu	12	3.07	0.0050	13.22
	Cu–O	6	3.59	0.0056	6.75

CN; coordination number, R; interatomic distance, $\Delta\sigma^2$; Debye–Waller factor; ΔE_0; energy shift.

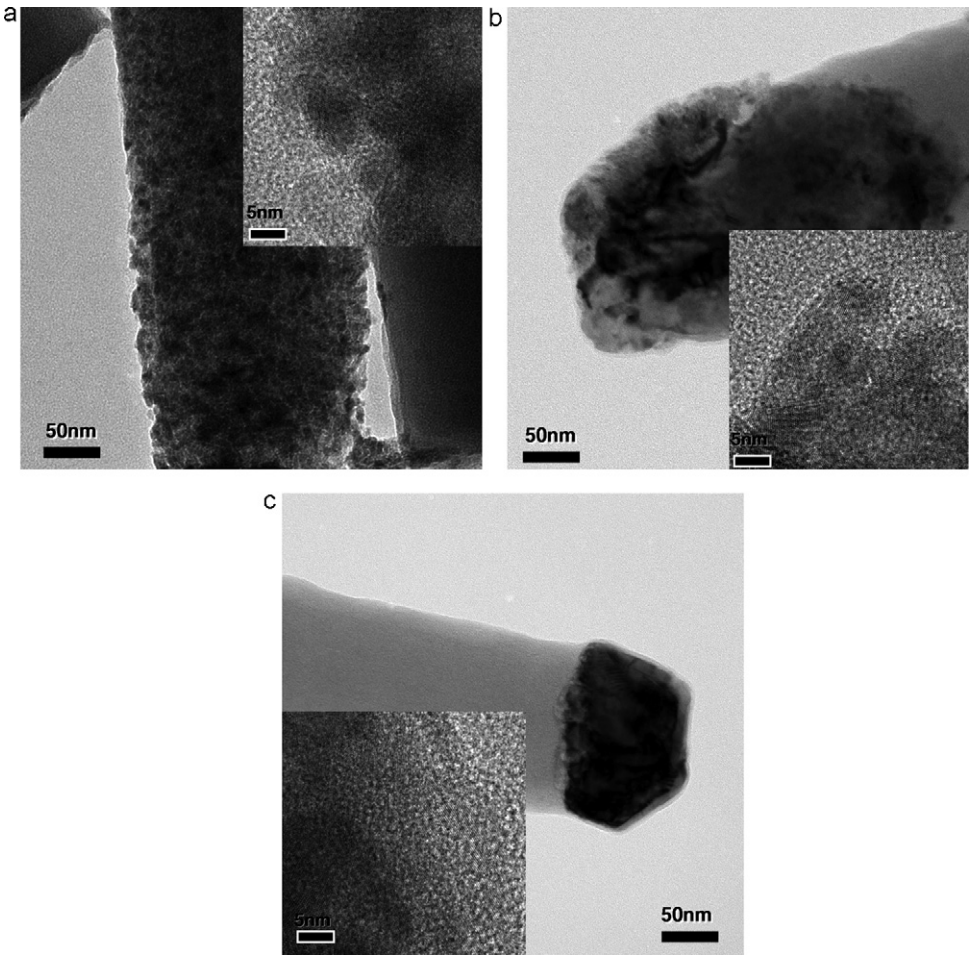

Fig. 3. HR-TEM images of Cu_xO/CNFs with various temperatures; (a) Cu_xO/CNF-700, (b) Cu_xO/CNF-800, and (c) Cu_xO/CNF-900.

of the electrochemical performance, it can be easily guessed that such morphology leads to the improvement of the specific capacity as well as the cycle retention. For Cu_xO/CNF-800, the *R* and *CN* corresponding to Cu–O bond in the first shell are 1.88 Å and 1.99 Å with *CN* of 1.7 and 1.4, those of corresponding to Cu–O bond in the second shell are 2.81 Å and 0.6, and those of corresponding to Cu–Cu bond in the third shell are 2.94 Å and 2.6, 3.04 Å and 2.7. The Cu_xO/CNF-800 represents an intermediate state between the disordered CuO structure and the Cu_2O structure, as mentioned in the plot of the $k^3\chi(k)$ of Fig. 4(b). By comparison with the structure of pure CuO, the number of oxygen in the first and second shell is insufficient as much as 0.9 and 1.4, respectively, and the number of Cu in third shell is deficient 3.5 as well. The *CN* of oxygen decreases as carbonization temperature increases from 700 to 800 °C, while that of Cu increases. The CNFs play an important role as a buffering agent that aids the distribution of the Cu_xO particles. Consequently, this transformation and degree of distribution of Cu_xO affect the electrochemical properties. For the Cu_xO/CNF-900, the *R* and *CN* of Cu–O bond in the first shell are 1.86 Å and 2.4, those of Cu–Cu bond in the second are 3.07 Å and 12, and those of Cu–O in the third shell are 3.59 Å and 4.8, respectively. Compared with the pure Cu_2O reference, the *R* and *CN* of Cu–O and Cu–Cu bonds in the first and second shells are similar, while the *CN* of Cu–Cu in the third shell is lower, although the bond lengths are equal. This means that the Cu_xO particles are agglomerated to promote their crystallinity during carbonization at 900 °C and that the CNFs did not prevent the growth of large crystal of Cu_xO. It can be expected that the atoms do not establish sufficient space so as to build the disordered structure due to high temperature, in spite of the buffering role of CNFs. In short, the structure around the Cu atoms in the carbon nanofibers is gradually transformed from CuO to Cu_2O with increasing carbonization temperature.

Fig. 5 shows the structural models of Cu_xO in the Cu_xO/CNFs, pure CuO and Cu_2O based on the distances and coordination numbers determined by EXAFS analysis. The Cu and oxygen atom are shown as yellow-green circles and red circles, respectively. For Cu_xO/CNF-700, the structure around Cu is nearly coincided with the CuO model as shown in Fig. 5(a), comprising of the disordered structure that the *CN* of Cu–Cu is lower than that of pure CuO. With the increase of the temperature up to 900 °C, the structure is transformed to Cu_2O as shown in Fig. 5(b). The *CN* of Cu–O decreases, but the *CN* of Cu–Cu increases due to high temperature. The oxidation state is changed from +2 to +1, as mentioned at the XANES results of Fig. 4(a). The information concerning the change of oxidation state indicates that the disordered CuO particle is transformed into Cu_2O with the increase of the temperature. As a consequence, it is easily surmised that Cu_xO/CNF-800 prepared at intermediate temperature is composed of the mixture of the disordered CuO and Cu_2O. In addition, the disordered structure with nanoparticles is closely related to the enhancement of both specific capacity and cycle performance [35–38].

Fig. 6 represents the electrical conductivity of Cu_xO/CNFs. The electrical conductivity gradually increases from 5.0×10^{-2} to 5.9×10^{-1} S cm^{-1} with the increase of temperature from 700 to 800 °C, and then abruptly increases to 1.1×10^{1} S cm^{-1} at 900 °C because the ratio of hydrogen to carbon (H/C ratio) is reduced by

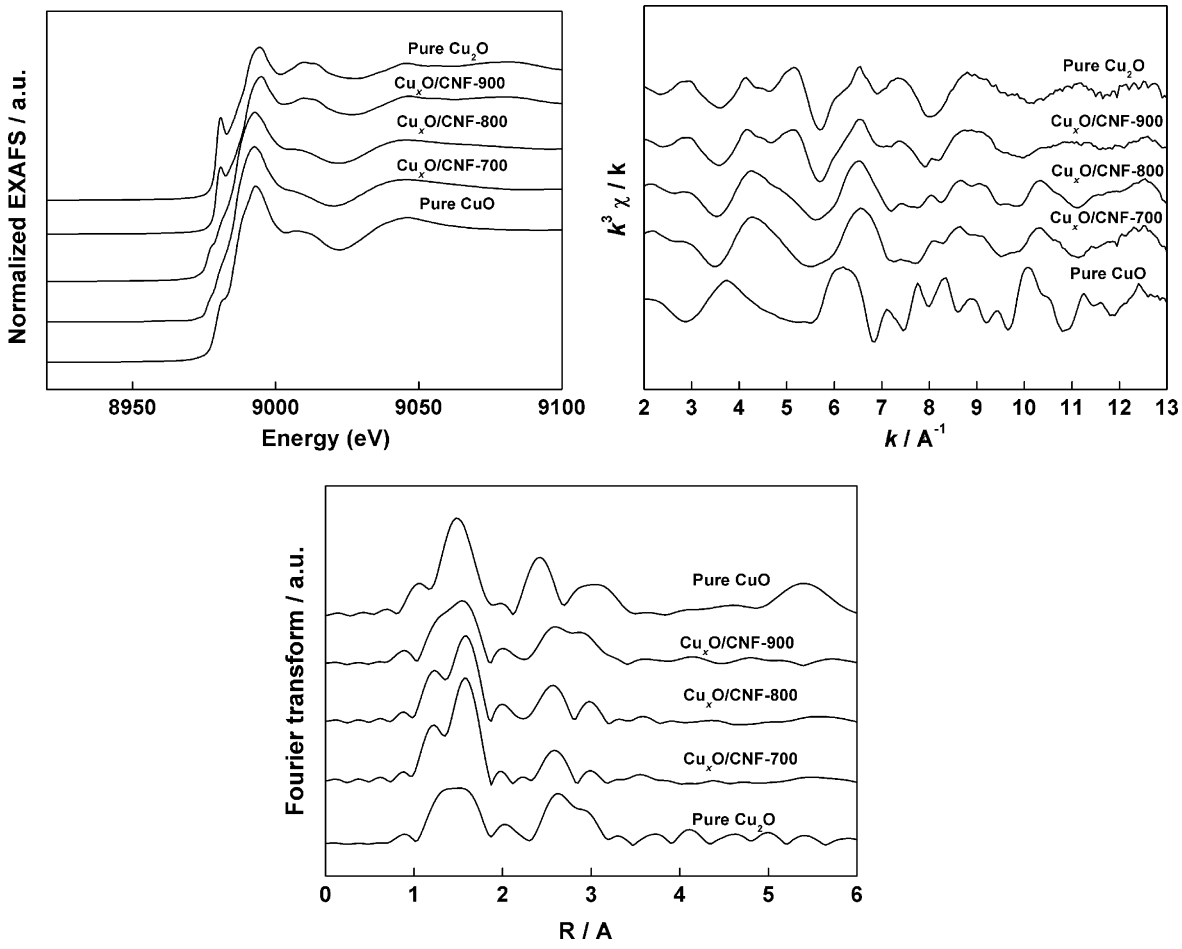

Fig. 4. EXAFS spectra of Cu_xO/CNFs with various temperatures; (a) XANES, (b) k^3-weighted EXAFS, and (c) Fourier transformed radial distribution.

the removal of hydrogen. The electrical conductivities of Cu_xO/CNFs represent high value because the CNF with one-dimensional pathway replenishes the deficient electrical conductivity of Cu_xO as a semiconductor [39,40]. The CNF plays a crucial role as buffering agent as well as electrical conductor in enhancing the electrochemical performance.

Fig. 7 shows the initial discharge–charge profiles of pure Cu_2O, CNF and the various Cu_xO/CNF electrodes in the voltage range 0.02–2.8 V using a cell assembled with Li metal. Scheme 2 illustrates the Li insertion and extraction in the Cu_xO-embedded carbon nanofibers in the discharge–charge profile of Fig. 7. The first discharge and charge capacities of pure Cu_2O were 504 and 102 mAh g^{-1}, respectively, and those of the pure CNF were 827 and 471 mAh g^{-1}, respectively. The irreversible capacity of pure Cu_2O with low electrical conductivity and large particle size is very large because Li_2O formed in the first discharging process is not decomposed. The irreversible capacity of CNF originates from the restriction of Li ion transfer through the formation of discontinuous pores. On the contrary, the Cu_xO/CNFs show much lower irreversible capacity than pure Cu_2O and CNF electrodes. The first discharge and charge capacity of Cu_xO/CNF-700, and Cu_xO/CNF-800 represent 860 and 580 mAh g^{-1}, and 687 and 494 mAh g^{-1}, respectively. The irreversible capacity of Cu_xO/CNF-700 is 280 mAh g^{-1}, while that of Cu_xO/CNF-800 is 193 mAh g^{-1}. In brief, the initial irreversible capacity improves with increasing temperature to 800 °C, while the first discharge capacity decreases. For Cu_xO/CNF-700, the initial discharge/charge capacity increases because of the disordered CuO structure, while the initial reversible capacity decreases due to low electrical conductivity. As for Cu_xO/CNF-800, the initial reversibility is much improved owing to high electrical conductivity, while the initial discharge/charge capacity decreases due to an intermediate state between the disordered CuO structure and the Cu_2O structure in CNF. The capacities of Cu_xO/CNF-700 and Cu_xO/CNF-800 composites have high value compared to the combined value of pure Cu_xO (30 wt%) and pure CNF (70 wt%) because of the behavior of well-distributed Cu_xO and buffering of CNF as the Cu_xO/CNFs nanocomposites. Basically, both Cu_xO/CNF-700 and

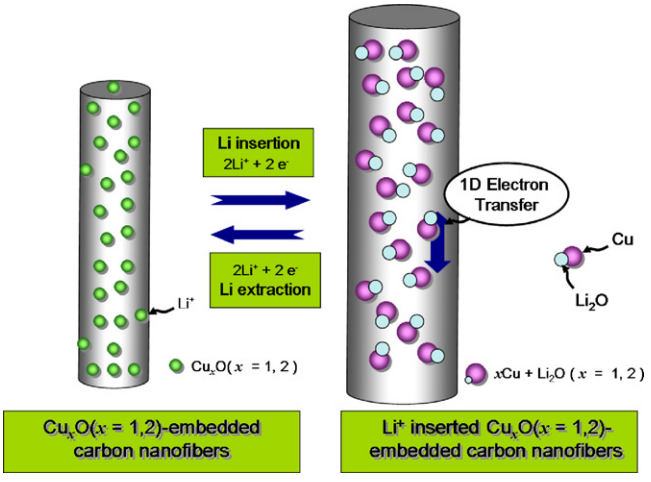

Scheme 2. Li insertion-extraction process of Cu_xO-embedded carbon nanofiber (Cu_xO/CNF).

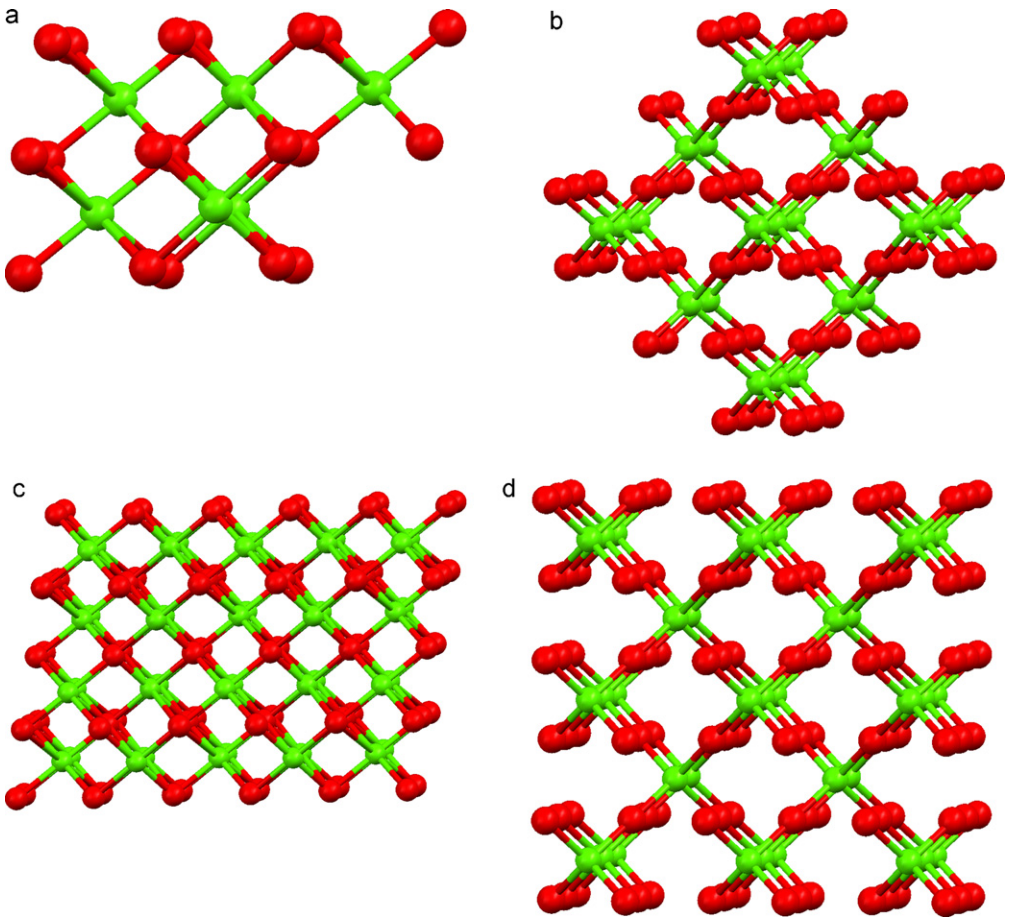

Fig. 5. The structural model of Cu_xO in Cu_xO/CNFs with various temperature, pure CuO (monoclinic), and Cu_2O (cubic) determined by EXAFS analysis: (a) Cu_xO/CNF-700, (b) Cu_xO/CNF-900, (c) pure CuO, and (d) pure Cu_2O.

Cu_xO/CNF-800 show excellent results for initial discharge/charge capacity and initial reversibility, as compared with other results. This improvement is originated from the morphology of CNF, the disordered structure of Cu_xO in the CNF, and the extreme distribution of the Cu_xO particles obtained by electrospinning. First, the specific capacity of the CNF is relatively high due to well-developed porous structures, despite large irreversible capacity. Second, the CNF prevents Cu_xO particles from agglomerating by acting as a buffering agent during cycling. Third, the CNF makes the electron transfer facilitate due to the role of electrical conductor. As a result, the CNF leads to the occurrence of Cu nanoparticles during discharging and promotes the conversion of Li_2O to Li during charging in the reaction Cu_xO ($x = 1, 2$) + $2Li^+ + 2e^- \leftrightarrow x$ Cu + 2 Li_2O. Fourth, the disordered Cu particles with short-range order play an important role in facilitating Li ion transfer because of their extremely small size. For the Cu_xO/CNF-900, the initial discharge and charge capacity represent 700 and 370 mAh g^{-1}, showing high irreversible capacity with low specific capacity com-

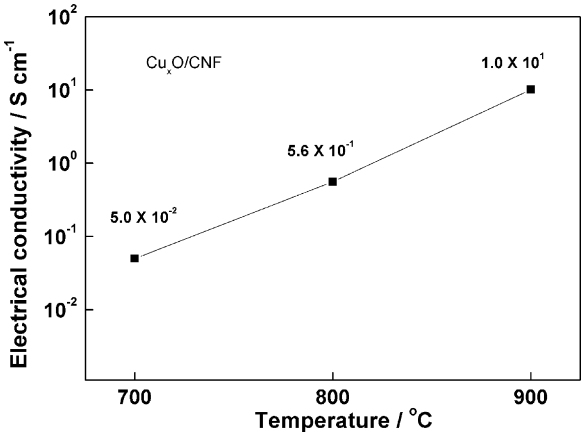

Fig. 6. Variations of electrical conductivities for Cu_xO/CNFs with various temperatures.

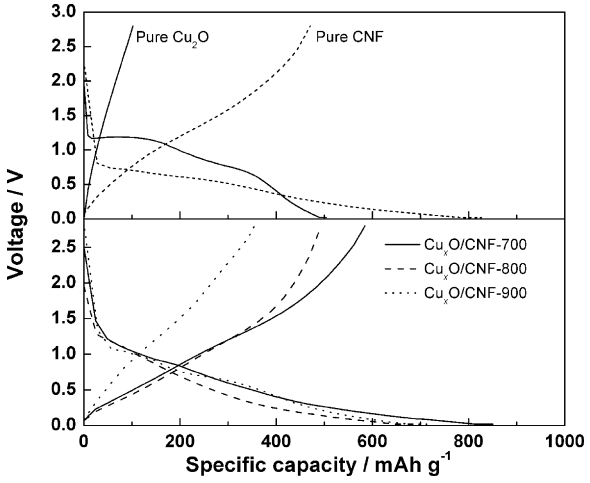

Fig. 7. Voltage profiles of the Cu_xO/CNFs with various temperatures in 1 M $LiPF_6$/EC/DMC at 0.5 mA cm^{-2}.

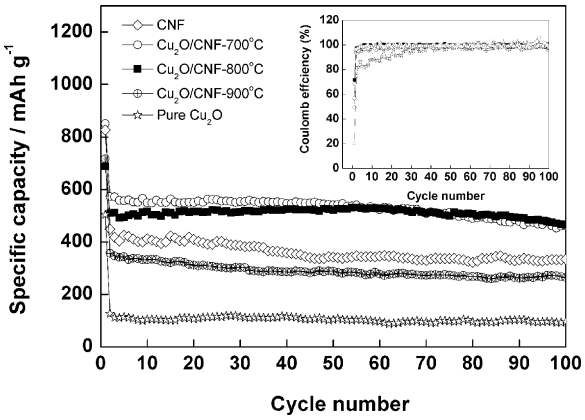

Fig. 8. Cycle performance and coulomb efficiency of the Cu_xO/CNFs with various temperatures at 0.5 mA cm^{-2} in 1 M $LiPF_6$/EC/DMC.

pared to other Cu_xO/CNFs, because of the agglomeration of Cu_2O. This is caused by large particle of Cu_xO and difficulty of decomposition of Li_2O during discharge process, despite high electrical conductivity.

Fig. 8 shows the cycling performances and coulomb efficiencies of pure Cu_2O, CNF and the Cu_xO/CNFs. Both Cu_xO/CNF-700 and Cu_xO/CNF-800 show high discharge capacities and excellent cycle retention, while the specific capacity and cycle retention of Cu_xO/CNF-900 is maintained at *ca.* 290 mAh g^{-1} from the second cycle, after dropping abruptly in the initial cycle. The capacity of pure CNF decreases to 336 mAh g^{-1} and those of pure Cu_2O abruptly decreases to 92 mAh g^{-1} in the 100th cycle. For pure Cu_2O powder, the discharge capacities of the initial, second, 50th and 100th cycle show 500, 126, 103, and 92 mAh g^{-1}, respectively. The discharge capacity of pure Cu_2O through all cycles is much lower than the theoretical value due to its large irreversible capacity. The coulomb efficiency of pure Cu_2O in the initial cycle is only 20%, and then is below about 98% at the 40th cycle. For pure CNF, the discharge capacities of the initial, second, 50th and 100th cycles are 826, 448, 341, and 336 mAh g^{-1}, respectively. The discharge capacity of pure CNF continuously decreases due to the discontinuous pores. The coulomb efficiency of pure CNF in the initial cycle exhibits 58%. In contrast, the Cu_xO/CNFs except for Cu_xO/CNF-900 represent excellent cycle performance with the excellent specific discharge capacity. The specific discharge capacity of Cu_xO/CNF decreases slightly due to well distribution of extremely small particles and the disordered structure of Cu_xO with the increase of tempera-

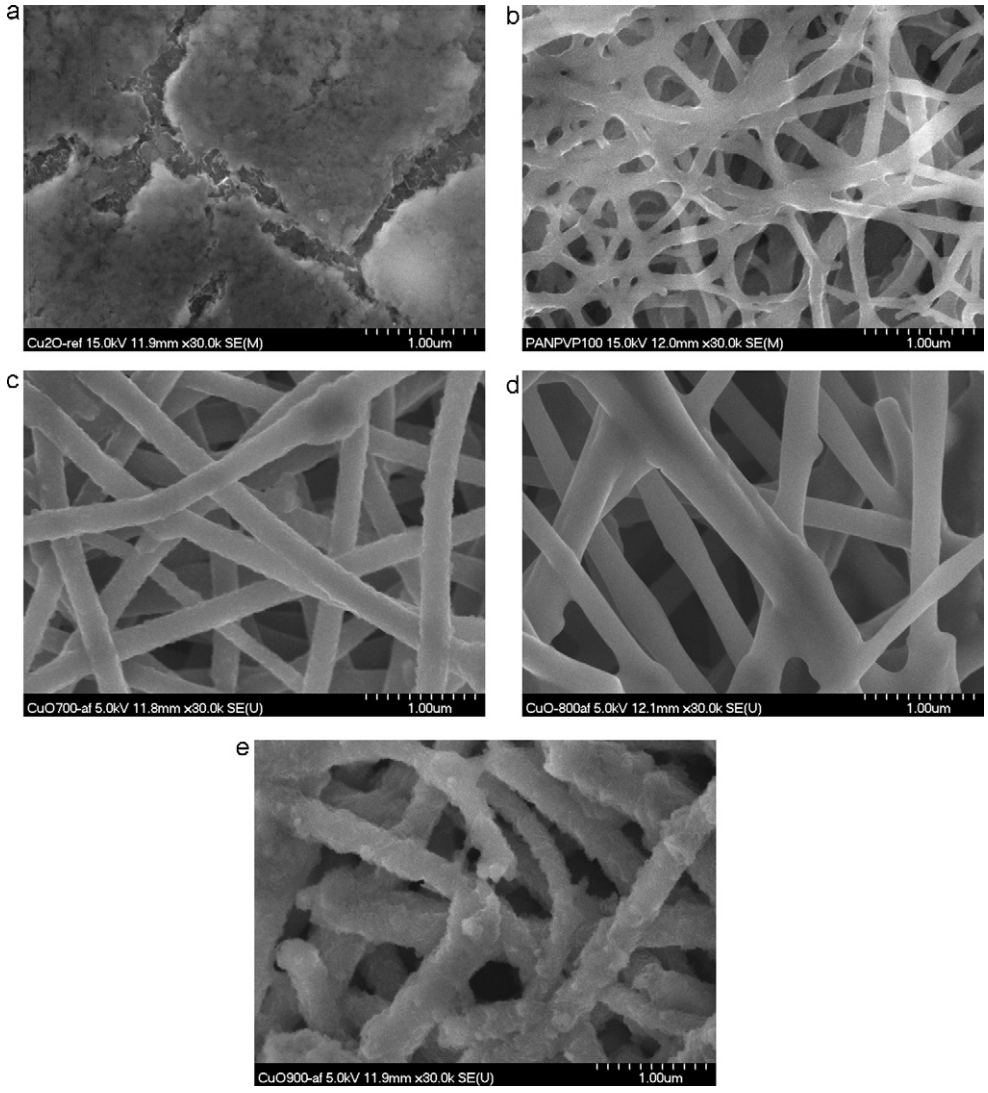

Fig. 9. SEM images of pure Cu_2O, pure CNF, Cu_xO/CNF with various temperatures after 100th cycle: (a) pure Cu_2O, (b) pure CNF (c) Cu_xO/CNF-700, (d) Cu_xO/CNF-800, and (e) Cu_xO/CNF-900.

ture from 700 to 800 °C, and then drastically decreases at 900 °C owning to large agglomeration of Cu_xO particles. The coulomb efficiencies of Cu_xO/CNF-700 and Cu_xO/CNF-800 in the initial cycle show very high values of 68 and 75%, respectively, and reach almost 100% from the second cycle. The discharge capacities of all the Cu_xO/CNFs through 100 cycles are much higher than the theoretical capacity of Cu_2O. For both Cu_xO/CNF-700 and Cu_xO/CNF-800 showing the excellent electrochemical performance, the discharge capacities of initial, second, 50th and 100th cycle for Cu_xO/CNF-700 represent 850, 572, 540, and 461 mAh g^{-1}, respectively, while those of Cu_xO/CNF-800 display 687, 508, 520, and 464 mAh g^{-1}, respectively. The excellent discharge capacity and cycle retention originates from the excellent distribution of Cu_xO nanoparticles in the carbon nanofibers due to electrospinning. Interestingly, their discharge capacities gradually decrease until the 10th cycle, and then steadily increase between the 20th and 70th cycle. This means that most metal particles in Cu_xO/CNF are participated in the electrochemical process. For Cu_xO/CNF-900, the electrochemical performance is the lowest among Cu_xO/CNFs, and its discharge capacity of initial, second, 50th and 100th cycle shows 700, 360, 305, and 285 mAh g^{-1}, respectively, dropping off abruptly at initial cycle. This is because the Cu_xO particles are large and agglomerated with an enhanced degree of crystallinity despite the CNF acting as a buffering agent and the Cu_xO/CNF-900 having higher electrical conductivity. This is because the Cu_xO particles are largely agglomerated with an enhanced degree of crystallinity, in spite of high electrical conductivity and buffering effect of CNF. As a consequence, the coulomb efficiency of the Cu_xO/CNF-900 decreases to 48% in the initial cycle.

Fig. 9 shows the surfaces of the pure Cu_2O, pure CNF and Cu_2O/CNF electrodes after the 100th cycle. For pure Cu_2O, the evidence is observed that Cu_2O particles are deeply agglomerated with the cracked appearance. Pure CNF keeps an interconnected structure without deformation of the fiber during Li ion insertion and extraction due to their porous structures. Both Cu_xO/CNF-700 and Cu_xO/CNF-800 maintains the shape of fibers forming the rounded contour by swelling the electrolyte because of porous structure of CNF with well-distributed Cu_xO particles. In brief, the porous structure of CNF easily alleviates the strain caused by volume expansion during Li-ion insertion and extraction. This phenomenon deeply affects the improvement of electrochemical performance such as the specific capacity and cycle retention and coulomb efficiency due to the improvement of charge transfer by large active electrochemically surface site, more decomposition of Li_2O by the improvement of electrical conductivity, and the increased ion transfer by large uptake of electrolyte. The Cu_xO/CNF-900 is formed as the partially broken fiber of the silkworm-like appearance with large granular lump because of the volume expansion by the development of agglomeration of Cu_xO, originating in the high carbonization temperature. This brings about the deterioration of the electrochemical performance.

4. Conclusions

The Cu_xO-embedded carbon nanofibers (Cu_xO/CNFs) were synthesized by electrospinning and thermal treatment. Both Cu_xO/CNF-700 and Cu_xO/CNF-800 show disordered CuO and Cu_2O structures, with excellent distribution of metal oxide particles. The Cu_xO/CNF-900 shows Cu_2O structure nearly without the disordered formation. This disordered structure leads to enhanced electrochemical performance because CNF hinders the formation of large Cu_xO structures. The improved electrochemical performance originates from the morphology of the CNF, the disordered Cu_xO structure, and the extreme distribution of Cu_xO particles. Both Cu_xO/CNF-700 and Cu_xO/CNF-800 shows excellent discharge capacities and cycle retention, while the Cu_xO/CNF-900 decreases electrochemical performance caused by the agglomeration of particles. Even in the initial cycle, the coulomb efficiency of Cu_2O/CNF-700 and Cu_2O/CNF-800 reaches 68% and 75%, respectively. The discharge capacities of 100th cycle for Cu_xO/CNF-700 and Cu_xO/CNF-800 keep 455 and 464 mAh g^{-1}, respectively.

Acknowledgments

This research was financially supported by the Ministry of Education, Science Technology (MEST) and National Research Foundation of Korea (NRF) through the Human Resource Training Project for Regional Innovation.

References

[1] W.L. Yao, J. Yang, J.L. Wang, Y.N. Nuli, J. Electrochem. Soc. 155 (12) (2008) A903.
[2] W.-M. Zhang, X.-L. Wu, J.-S. Hu, Y.-G. Guo, L.-J. Wan, Adv. Funct. Mater. 18 (24) (2008) 3941.
[3] P. Poizot, S. Laruelle, S. Grugeon, L. Dupont, J.-M. Tarascon, Nature 407 (2000) 496.
[4] H. Liu, G.X. Wang, J.S. Park, J.Z. Wang, H.K. Liu, C. Zhang, Electrochim. Acta 54 (6) (2009) 1733.
[5] Y.H. Lee, I.C. Leu, S.T. Chang, C.L. Liao, K.Z. Fung, Electrochim. Acta 50 (2–3) (2004) 553.
[6] J.Y. Xiang, J.P. Tu, X.H. Huang, Y.Z. Yang, J. Solid State Electrochem. 12 (7–8) (2008) 941.
[7] J. Morales, L. Sanchez, F. Martin, J.R. Ramos-Barrado, M. Sanchez, Electrochim. Acta 49 (26) (2004) 4589.
[8] J.C. Park, J.H. Kim, H.S. Kwon, H.J. Song, Adv. Mater. 21 (7) (2009) 803.
[9] Y.Y. Hu, X.T. Huang, K. Wang, J.P. Liu, J. Jiang, R.M. Ding, X.X. Ji, X. Li, J. Solid State Chem. 18 (2010) 662.
[10] J. Morales, L. Sanchez, S. Bijani, L. Martinez, M. Gabas, J.R. Ramos-Barrado, Electrochem. Solid-State Lett. 8 (3) (2005) A159.
[11] J.Y. Xiang, J.P. Tu, Y.F. Yuan, X.L. Wang, X.H. Huang, Z.Y. Zeng, Electrochim. Acta 54 (2009) 1160.
[12] F.-S. Ke, L. Huang, G.-Z. Wei, L.-J. Xue, J.-T. Li, B. Zhang, S.-R. Chen, X.-Y. Fan, S.-G. Sun, Electrochim. Acta 54 (2009) 5825.
[13] C. Xu, X. Wang, L.C. Yang, Y.P. Wu, J. Solid State Chem. 182 (2009) 2486.
[14] G.T. Wu, C.S. Wang, X.B. Zhang, H.S. Yang, Z.F. Qi, W.Z. Li, J. Power Sources 75 (1998) 175.
[15] J.Y. Xiang, J.P. Tu, J. Zhang, J. Zhong, D. Zhang, J.P. Cheng, Electrochem. Commun. 12 (2010) 1103.
[16] C.Q. Zhang, J.P. Tu, X.H. Huang, Y.F. Yuan, X.T. Chen, F. Mao, J. Alloys Compd. 441 (1–2) (2007) 52.
[17] J.Y. Xiang, J.P. Tu, Y.F. Yuan, X.H. Huang, Y. Zhou, L. Zhang, Electrochem. Commun. 11 (2) (2009) 262.
[18] L. Wang, Y. Yu, P.C. Chen, D.W. Zhang, C.H. Chen, J. Power Sources 183 (2008) 717.
[19] L. Wang, Y. Yu, P.C. Chen, C.-H. Chen, Scripta Mater. 58 (2008) 405.
[20] Y.H. Zhang, M.L. Toebes, A. Van der Eerden, W.E. O'Grady, K.P. De Jong, D.C. Koningsberger, J. Phys. Chem. B 108 (48) (2004) 18509.
[21] H.C. Choi, S.Y. Lee, S.B. Kim, M.G. Kim, M.K. Lee, H.J. Shin, J.S. Lee, J. Phys. Chem. B 106 (2002) 9252.
[22] A. Yanase, H. Komiyama, Surf. Sci. 248 (1–2) (1991) 11.
[23] M. Khitouni, R. Daly, M. Mhadhbi, A. Kolsi, J. Alloys Compd. 475 (1–2) (2009) 581.
[24] C.W. Hao, Y. Zhao, Y. Zhou, L.J. Zhou, Y.Z. Xu, D.J. Wang, D.F. Xu, J. Polym. Sci. B Polym. Phys. 45 (13) (2007) 1589.
[25] C.E. Hoppe, M. Lazzari, I. Pardinas-Blanco, M.A. Lopez-Quintela, Langmuir 22 (16) (2006) 7027.
[26] T.J. Hashimoto, K.J. Saijo, M.F. Harada, N.K. Toshima, J. Chem. Phys. 109 (13) (1998) 5627.
[27] X.Q. Wang, J.C. Hanson, A.I. Frenkel, J.-Y. Kim, J.A. Rodriguez, J. Phys. Chem. B 108 (2004) 13667.
[28] Y. Xi, C.-G. Hu, P.-X. Gao, R.-S. Yang, X.-S. He, X. Wang, B.-Y. Wan, Mater. Sci. Eng. B 166 (2010) 113.
[29] D.A. Firmansyah, T.I. Kim, S.K. Kim, K. Sullivan, M.R. Zachariah, D.G. Lee, Langmuir 25 (12) (2009) 7063.
[30] J.-N. Nian, C.-C. Tsai, P.-C. Lin, H.S. Teng, J. Electrochem. Soc. 156 (7) (2009) H567.
[31] Y.-J. Huang, H.P. Wang, J.-F. Lee, Chemosphere 50 (2003) 1035.
[32] D.M. Pickup, I. Ahmed, V. FitzGerald, R.M. Moss, K.M. Wetherall, J.C. Knowles, M.E. Smith, R.J. Newport, J. Non-Crystal Solids 352 (2006) 3080.
[33] R.P. Wijesundera, M. Hidaka, W. Siripala, S.-H. Choi, N.E. Sung, M.G. Kim, J.M. Lee, Phys. Stat. Sol. (B) 243 (2006) 1791.
[34] J.H. Lee, T. Yano, S. Shibata, A. Nukui, M. Yamane, J. Non-Crystal. Solids 277 (2000) 155.

[35] J.T.S. Irvine, P.A. Connor, Electrochim. Acta 47 (2002) 2885.
[36] A.J. Kropf, H. Tostmann, C.S. Johnson, J.T. Vaughey, M.M. Thackeray, Electrochem. Commun. 3 (2001) 244.
[37] S.I. Lee, S.K. Yoon, C.M. Park, J.M. Lee, H.S. Kim, D.M. Im, S.G. Doo, H.J. Sohn, Electrochim. Acta 54 (2008) 364.
[38] C.H. Chen, B.J. Hwan, J.S. Do, J.H. Weng, M. Venkateswarlu, M.Y. Cheng, R. Santhanam, K. Ragavenran, J.F. Lee, J.M. Chen, D.G. Liu, Electrochem. Commun. 12 (2010) 496.
[39] T. Ito, H. Yamaguchi, K. Okabe, T. Masumi, J. Mater. Sci. 33 (1998) 3555.
[40] L.C. Bourne, P.Y. Yu, A. Zettl, M.L. Cohen, Phys. Rev. B 40 (1989) 10973.